AIP | Journal of Applied Physics

Engineering domain structures in nanoscale magnetic thin films via strain

Jia-Mian Hu, T. N. Yang, L. Q. Chen, and C. W. Nan

Citation: Journal of Applied Physics **114**, 164303 (2013); doi: 10.1063/1.4826491
View online: http://dx.doi.org/10.1063/1.4826491
View Table of Contents: http://scitation.aip.org/content/aip/journal/jap/114/16?ver=pdfcov
Published by the AIP Publishing

Engineering domain structures in nanoscale magnetic thin films via strain

Jia-Mian Hu,[1,a)] T. N. Yang,[2] L. Q. Chen,[1,2] and C. W. Nan[1,a)]
[1]*School of Materials Science and Engineering and State Key Lab of New Ceramics and Fine Processing, Tsinghua University, Beijing 100084, China*
[2]*Department of Materials Science and Engineering, The Pennsylvania State University, University Park, Pennsylvania 16802, USA*

(Received 8 July 2013; accepted 6 October 2013; published online 22 October 2013)

We study the strain effects on magnetic domain stability and dynamics in nanoscale magnetic thin films using phase-field simulations. Numerous strain-stabilized single-/multi-domain states are discovered, including various magnetic vortices with circular in-plane domains. Furthermore, a strain-domain stability map was constructed, displaying the stable magnetic domain and domain wall structures as a function of biaxial isotropic and anisotropic in-plane strains at room temperature. The present work provides useful guidelines for a precise engineering and experimental observation of domain structures in nanoscale magnetic thin films and a promising scheme towards a low-power and local control over magnetic domain structures. © *2013 AIP Publishing LLC*. [http://dx.doi.org/10.1063/1.4826491]

I. INTRODUCTION

Strain is a critically important factor in many structural phase transformations.[1] Particularly, thin films offer the opportunity to bear large strains far beyond where their bulk counterparts would crack.[2] This would enable us to tune a specific property of a chosen material in the thin film form.[3–5] For example, in magnetic thin films, magnetization/magnetic domain can be switched between an in-plane (IP) and out-of-plane (OOP) direction under isotropic biaxial IP strains[6] or rotate within the film plane under anisotropic biaxial IP strains[7] which can further be utilized to develop low-power, mechanically controlled spintronic devices.[8–13] However, the details of strain-magnetization coupling in magnetic thin films deserve further study[14] to accelerate the real application of such novel devices, especially in nanoscale thin-film magnets which are highly desirable for device miniaturization.

A nanoscale magnetic thin film would be either in a single-domain or multi-domain state resulting from the competing exchange and magnetostatic fields,[15] which can be understood using micromagnetic simulations.[16,17] However, micromagnetic approach normally cannot describe the mechanical boundary condition in nanoscale magnetic thin films, i.e., either homogeneously or inhomogeneously (e.g., in an isolated island of film with non-uniform stress distribution[18,19]) constrained by a substrate. These boundary conditions have remarkable influences especially when the magnetoelastic coupling is strong.

By combing micromagnetics with the microelasticity theory of Khachaturyan,[1] Zhang *et al.*[20] developed a phase-field model to study the magnetic domain structures in bulk alloys with large magnetostriction (i.e., the inverse magnetoelastic coupling) as well as the strain response of ferromagnetic shape-memory alloy.[21] In this article, we extend this model to nanoscale magnetic thin films by incorporating corresponding elastic and magnetostatic boundary conditions (Sec. II), whereby the strain effects on the magnetic domain stability and dynamics are investigated. Numerous strain-stabilized single-domain and multi-domain states are discovered including an explicit in-plane vortex domain state. It is further shown that such vortex domain structure can also exist and be manipulated by strain in both the isolated magnetic nanoisland and continuous nanoscale thin film (i.e., only the film thickness is in the nanometer range). Based on the simulations, we construct a strain-domain stability map for homogeneously constrained nanoscale magnetic thin films, which displays the stable magnetic domain and domain wall structures as a function of isotropic and anisotropic biaxial IP strains at room temperature. The map should provide a solid basis for a designated control over domain patterns in nanoscale magnetic thin films via strain.

II. MODEL

For illustration, a polycrystalline Ni nanoscale thin film, which is one of the most representative transition-metal ferromagnets and has been widely used in electronic devices (e.g., the electrodes of the multilayer capacitors[22,23]), is chosen as a model material system also due to its robust magnetoelastic coupling.[24]

In the phase-field approach, the magnetic domain structure is described by the spatial distribution of the local magnetization vectors $\mathbf{M} = M_s\mathbf{m} = M_s(m_1, m_2, m_3)$, where M_s and $m_i (i = 1, 2, 3)$ represent the saturation magnetization and the direction cosine, respectively. The temporal evolution of the magnetization configuration at room-temperature ($T = 298$ K) and thus the domain structure is governed by the Landau-Lifshitz-Gilbert (LLG) equation, i.e.,

$$(1+\alpha^2)\frac{\partial \mathbf{M}}{\partial t} = -\gamma_0 \mathbf{M} \times \mathbf{H_{eff}} - \frac{\gamma_0 \alpha}{M_s}\mathbf{M} \times (\mathbf{M} \times \mathbf{H_{eff}}). \quad (1)$$

Here γ_0 and α are the gyromagnetic ratio and the damping constant, which are taken as -2.42×10^5 (A s)$^{-1}$ and 0.028

a)Authors to whom correspondence should be addressed. Electronic addresses: jiamian.hu1987@gmail.com and cwnan@tsinghua.edu.cn

for Ni,[25] respectively. $\mathbf{H_{eff}}$ is the effective magnetic field, given as $\mathbf{H_{eff}} = -(1/\mu_0 M_s)(\partial F_{tot}/\partial \mathbf{m})$. Here μ_0 denotes the vacuum permeability, and F_{tot} is the total free energy of an isotropic polycrystalline magnetic film, expressed by

$$F_{tot} = F_{ms} + F_{ex} + F_{elas}, \tag{2}$$

where F_{ms}, F_{ex}, and F_{elas} are the magnetostatic, magnetic exchange, and elastic energy, respectively. Note that we do not use the Laudau-Lifshitz-Bloch (LLB) equation with a stochastic term which could better describe the thermodynamic equilibrium and nonequilibrium behaviors of magnetic domain states at nonzero temperature,[26–28] mainly due to the high Curie temperature T_c of the Ni (around 628 K) and the resultant conserved magnetization vector length at room temperature. In this case, the temperature-independent LLG equation should be applicable if tentatively not considering the possible thermal excitation which is more likely to happen for the magnetic domain states around the *phase boundaries* as will be discussed later.

In Eq. (2), F_{elas} is given by

$$F_{elas} = \frac{1}{2}\int c_{ijkl} e_{ij} e_{kl} dV = \frac{1}{2}\int c_{ijkl}(\varepsilon_{ij} - \varepsilon^0_{ij})(\varepsilon_{kl} - \varepsilon^0_{kl}) dV, \tag{3}$$

where e_{ij} is elastic strain, c_{ijkl} the elastic stiffness tensor, and ε^0_{ij} the stress-free strainassociated with local magnetization change,[20] i.e.,

$$\varepsilon^0_{ij} = \frac{3}{2}\lambda_{100}\left(m_i m_j - \frac{1}{3}\right) \quad \text{or} \quad \frac{3}{2}\lambda_{111} m_i m_j (i \neq j), \tag{4}$$

where λ_{100} ($=\lambda_{111} = \lambda_s$) denotes the magnetostriction constant. Note that all the strain components as well as magnetization vectors are defined in a rectangular coordinate system $\boldsymbol{x} = (x_1, x_2, x_3)$ in this work, with the x_1, x_2, and x_3 axes along the three principle [100], [010], and [001] axes. ε_{ij} is the total strain that can be represented as the sum of homogenous and heterogeneous strains following Khachaturyan's theory of microelasticity,[1] i.e., $\varepsilon_{ij} = \overline{\varepsilon_{ij}} + \eta_{ij}$. The heterogeneous strain η_{ij} is defined in such a way so that $\int_V \eta_{ij} dV = 0$, and the homogeneous strain $\overline{\varepsilon_{ij}}$ describes the macroscopic deformation of the magnetic thin film. For the magnetic thin films whose lateral length are fully constrained by a stiff substrate of similar size, the complete relaxation of the average IP stress requires $\langle \varepsilon^0_{11} \rangle = \langle \overline{\varepsilon_{11}} \rangle = e_{s1}$ and $\langle \varepsilon^0_{22} \rangle = \langle \overline{\varepsilon_{22}} \rangle = e_{s2}$, where the angle brackets represent the volume average. Thanks to the magnetoelstic coupling [Eq. (4)], various stable magnetic domain structures would emerge upon such biaxial IP strains e_{s1} and e_{s2}. For the present polycrystalline Ni film with an incoherent film-substrate interface, such biaxial in-plane strains could arise from the grain boundaries during growth of Volmer-Weber thin films,[29,30] the thermal mismatch with the substrate,[31] and electromechanical actuations based on a piezoelectric substrate, for instance, the lead magnesium niobate-lead titanate (PMN-PT[24,32–34]) single crystals with ultrahigh piezoelectric response.[35] For simplicity, we tentatively do not consider possible plastic deformation and dislocation generation such that these biaxial strains can be applied to the constrained magnetic thin films without loss. By further considering an OOP stress-free boundary condition for typical film-substrate system[31] assuming elastic homogeneity, the elastic energy F_{elas} can be calculated by combining the microelasticity theory[1] with the Stroh's formalism of anisotropic elasticity.[36]

In addition, the substrate constraint can be partially relieved when cutting the thin film into an island, leading to a non-uniform stress distribution,[18,19] and the corresponding elastic energy is calculated by considering a three-phase model,[37] i.e., an island, a substrate, and gas, based on an perturbation method for elastic inhomogeneous systems.[38,39] The stress-free boundary conditions along the surfaces of the island can be automatically satisfied by setting the elastic constants as zero for the gas phase.

The magnetostatic energy F_{ms} can be expressed as[20]

$$F_{\mathrm{ms}} = -\frac{1}{2}\mu_0 M_s \int \mathbf{H_d} \cdot \mathbf{m} dV, \tag{5}$$

where the $\mathbf{H_d}$ denotes the stray field. For the investigated three-dimensional (3D) nanoscale magnetic thin films whose actual sample sizes are comparable to the simulation system size as shown below, $\mathbf{H_d}$ is numerically calculated by employing a finite-size magnetostatic boundary condition previously developed for a 3D array of ferromagnetic cubes.[40] While for the bulk magnets like the case in Ref. 20 or continuous nanoscale magnetic thin films whose real sizes are much larger than the simulation system size, a periodic magnetostatic boundary condition should be a good approximation.

Finally, the isotropic exchange energy F_{ex} depends on the gradients of the local magnetization vectors, i.e.,

$$F_{\mathrm{ex}} = A\int[(\nabla m_1)^2 + (\nabla m_2)^2 + (\nabla m_3)^2] dV, \tag{6}$$

where A is the exchange constant taken as 8.6×10^{-12} J/m for Ni from Ref. 41.

The temporal evolution of the local magnetization and thus the domain structures in the Ni films are obtained by numerically solving the LLG equation using the Gauss-Seidel projection method.[42] The film-substrate system is discretized into a 3D array of cubic cells of $64\Delta x \times 64\Delta y \times 72\Delta z$. The thickness of the substrate and the magnetic thin film/island are set as $h_s = 30\Delta z$ and $h_f = 35\Delta z$ (or $15\Delta z$), respectively, while the rest layers are vacuum. The Δx, Δy, and Δz denote the grid size of the simulation system, which, for instance, can all be taken as 1 nm in real space to represent an actual system size of $64 \times 64 \times 72\,\mathrm{nm}^3$. By further varying the simulation system size and/or the grid size of each unit cell, the magnetic thin films with different lateral sizes and thicknesses can be treated.[10,11] By taking the thickness d of the Ni film as 35(15) nm, the contribution of the magnetic interface anisotropy can be neglected, because it is inversely proportional to d and hence only becomes significant in ultrathin (several monolayers) metallic magnetic thin films.[43] Each simulation starts with an initial random configuration with arbitrary magnetization orientations and proceeds for long enough time to reach a

strain-stabilized domain structure which should correspond to a near equilibrium state, i.e., no significant changes happen for prolonged annealing during film growth and/or after an external strain was applied. The room-temperature elastic, and magnetostriction constant (i.e., $\lambda_s = -32.9$ ppm) of the polycrystalline Ni film used for simulation were taken from Ref. 7.

III. RESULTS AND DISCUSSIONS

A. Strain-domain stability map in homogeneously constrained nanoscale magnetic thin films

Figure 1(a) presents several strain-stabilized magnetic domain states at room temperature in polycrystalline Ni films of $64 \times 64 \times 35$ nm^3, including three tetragonal (a_1, a_2, c) and three orthorhombic (O_{12}, O_{13}, O_{23}) domains. Note that single-domain structures are observed due to the dominant short-range exchange energy in magnetic nanostructures of small geometric size.[11] Such different stable magnetization orientations in nanoscale thin-film magnets offer great design flexibility for magnetic device applications. Based on the simulation results, a strain-domain stability map, i.e., a graphic representation of stable domain structures as a function of moderate biaxial IP strains e_{s1} and e_{s2} within $\pm 1\%$, is established [Fig. 1(b)]. The sources of such biaxial IP strains have been discussed in Sec. II. Of interest to note is that both isotropic ($e_{s1} = e_{s2}$) and anisotropic ($e_{s1} \neq e_{s2}$) strains can be obtained by using piezoelectric substrates with different crystal orientations, e.g., the (001)[32,34] and (011)-oriented[24] PMN-PT, respectively. Particularly, if the magnetic thin film was grown on a ferroelectric bottom layer, the surface ferroelastic domain patterns could also provide controllable[44] IP structural strains that can be, at least partially,[45] transferred to the magnetic thin film during its growth. Thus, it is reasonable to believe that the IP strains e_{s1} and e_{s2} can be tailored experimentally such that most part of the stability map can be covered. However, most existing experimental efforts focus on the strain-domain correlation in continuous nanoscale magnetic thin films,[34,45–50] while for the 3D thin-film nanomagets herein, more explicit experimental observation are awaited despite an earlier exploration in a polycrystalline Ni film of $380 \times 150 \times 35$ nm^3 grown on a Pb(Zr,Ti)O$_3$ thick film (~ 1.28 μm).[19]

As shown in Fig. 1(b), the major part of the map consists of tetragonal (a_1, a_2, c) domains while the orthorhombic domains (O_{12}, O_{13}, O_{23}) appear as their intermediate phases. This is determined by the six-fold cubic symmetry of the magnetoelastic energy in isotropic magnets[51] which tends to align the magnetization along the three principle axes. There also exists a very small region occupied by a rhombohedral r domain ($M_1 \neq 0$, $M_2 \neq 0$, and $M_3 \neq 0$) in the map at the intersection of all the other phases. However, the rhombohedral domain and all the domain states around the phase boundaries in the map are very sensitive to the applied strains and would readily undergo thermal excitations[52,53] when the energy barrier between the two or more different domain states becomes comparable to the thermal activation energy kT, where k is the Boltzmann constant and T is the Kelvin temperature.[54] In addition, it is worth noting that the O_{12} domain exhibits a slightly larger area fraction in the map than the intermediate O_{13} and O_{23} domains, due to the demagnetization (magnetostatic) energy along the $\langle 001 \rangle$ direction which favors IP domain alignment. For the same reason, the IP tetragonal a_1 and a_2 domains take up a larger part in the map than the c domain, as shown in Fig. 1(b).

Shown in Fig. 2(a) are the strain-stabilized domain configurations in polycrystalline Ni films of larger size $192 \times 192 \times 35$ nm^3, which includes three tetragonal single phases (a_1, a_2, c), three binary phases ($a_1 + a_2$, $a_1 + c$, and $a_2 + c$), and one three phase mixtures ($a_1 + a_2 + c$). Note that the single-phases herein always contain two equivalent domain variants, say, the (M_1, 0, 0) and (-M_1, 0, 0) domains in the tetragonal a_1 phase, leading to the presence of multi-domain and domain wall structures. A seven-phase domain stability map is constructed likewise, as illustrated in Fig. 2(b). Compared to its single-domain counterpart [Fig. 1(b)], the mixed phases [analogously to the intermediate orthorhombic and rhombohedral phases in Fig. 1(b)] occupy a large part of the multi-domain stability map, along with much smoother phase boundaries [Fig. 2(b)]. This is mainly due to the presence of domain wall structures which reduce the magnetostatic energy such that the mixed phases become more energetically favorable. By contrast, the tetragonal

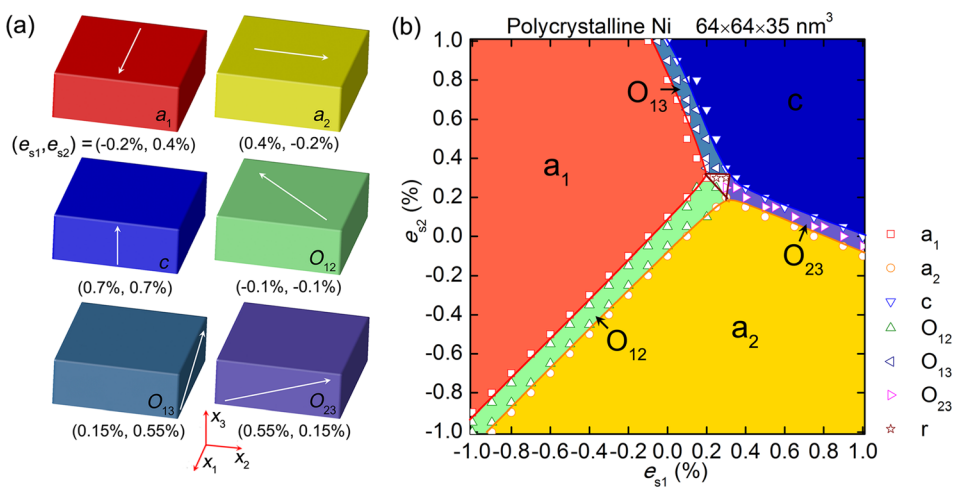

FIG. 1. (a) Strain-stabilized magnetic single-domain states in polycrystalline Ni films (homogeneously constrained) of $64 \times 64 \times 35$ nm^3. Phase definitions and the corresponding magnetizations: a_1 ($M_1 \neq 0$ and $M_2 = M_3 = 0$), a_2 ($M_2 \neq 0$ and $M_1 = M_3 = 0$), and c ($M_3 \neq 0$ and $M_1 = M_2 = 0$); O_{12} ($M_1 \neq 0$, $M_2 \neq 0$, and $M_3 = 0$), O_{13} ($M_1 \neq 0$, $M_3 \neq 0$, and $M_2 = 0$), and O_{23} ($M_2 \neq 0$, $M_3 \neq 0$, and $M_1 = 0$). The arrows indicate the magnetization orientations. (b) Its strain-domain stability map. The solid lines are eye guides for the phase boundaries.

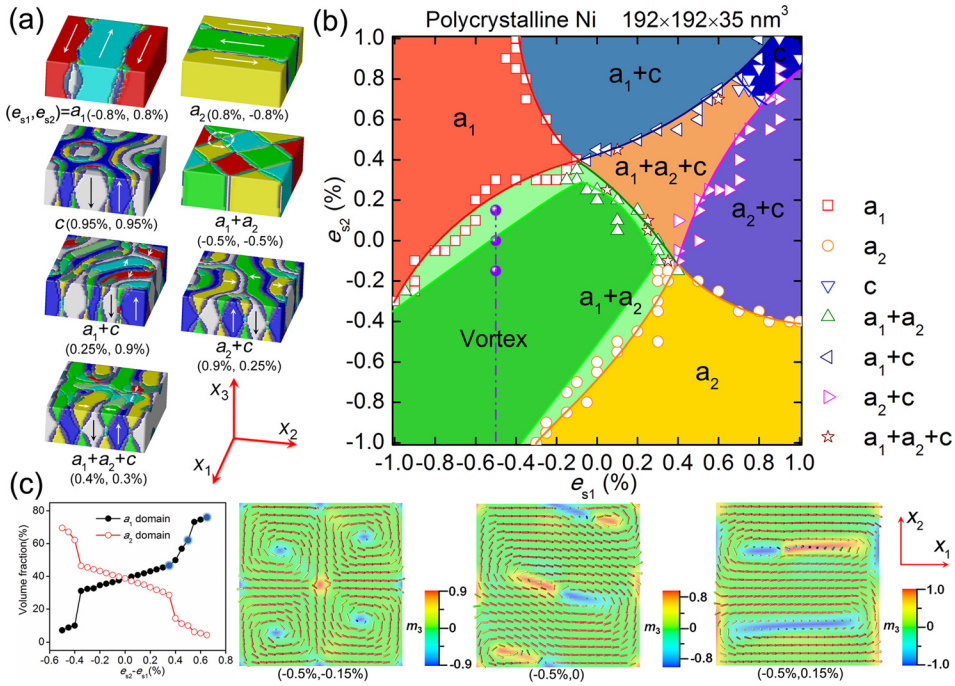

FIG. 2. (a) Strain-stabilized magnetic multi-domain states in polycrystalline Ni films (homogeneously constrained) of $192 \times 192 \times 35\,\text{nm}^3$. Each single-phase (e.g., a_1, a_2, c) contains two degenerate magnetization domains and corresponding domain wall structures. (b) Its strain-domain stability map. The solid lines are eye guides for the phase boundaries. (c) From left to right: the line graph shows the volume fractions of the in-plane domains a_1 and a_2 dependent on the in-plane strain difference e_{s1}-e_{s2}; the vector diagrams (top view) illustrate the typical magnetic configurations corresponding to the three solid spheres in the stability map. (Color bar) m_3 indicates the normalized magnetization in the out-of-plane x_3, i.e., the [001] direction.

single-phases (a_1, a_2, c) herein can only be stabilized under relatively large strains.

The obtained symmetric, seven-phase strain-domain stability maps [Figs. 1(b) and 2(b)] should be general for all homogeneously constrained isotropic (e.g., polycrystalline or amorphous) nanoscale magnetic thin films due to the cubic symmetry of the magnetoelastic anisotropy energy. However, the detailed structures and phase fractions of their comprising strain-stabilized domain states would vary from case to case, and are dependent on the specific geometric size. For instance, a thinner film (e.g., 15 nm) would favor IP domain alignment and thus larger parts of IP phases due to the enhanced OOP demagnetization energy.[54]

B. Vortex domain in nanoscale magnetic thin films and the strain manipulation

In the homogeneously constrained nanoscale magnetic thin films discussed above, the strain-stabilized magnetic multi-domain states [Fig. 2(a)] exhibit structural complexity in their domain wall structures,[54] with the typical domain wall length ranging from several to tens of nanometers, depending on the competition between the extrinsic elastic and the intrinsic exchange anisotropy energy.[15] Of particular interest, a typical IP vortex domain structure appears in the binary $a_1 + a_2$ phase (Fig. 2(a)), where all the spin vectors rotate gradually in the film plane in order not to lose too much exchange energy, but can significantly reduce the dipole-dipole magnetostatic energy.[55] Here we explore in details the strain manipulation of such vortex domain state. For illustration, we plot the region of vortex domain in its stability map [Fig. 2(b)], i.e., the highlighted area in the $a_1 + a_2$ phase. By fixing the IP strain e_{s1} as -0.5% [see the dashed-dotted line in Fig. 2(b)], the volume fractions of the IP a_1 and a_2 domains as a function of the IP strain difference e_{s2}-e_{s1} is shown in Fig. 2(c). As seen, the well-defined vortex structure appears between -0.35% and 0.35% of the e_{s2}-e_{s1} and would gradually evolve towards the striped a_1 domain if e_{s2}-e_{s1} further increases with enhanced IP elastic anisotropy along the x_2 axis, as directly illustrated by the three selected magnetic vector diagrams (corresponding to the solid spheres in the stability map) in Fig. 2(c) as well.

Such a vortex domain state can also be present in both isolated magnetic nanoislands with relieved substrate constraint[44]) and constrained continuous magnetic thin films (with a periodic magnetostatic boundary conditions, see Sec. II), as shown in Fig. 3. First, compared to the symmetric, multiple IP vortices in homogeneously constrained nanoscale magnetic thin films upon compressive IP strains of (-0.5%, -0.5%) [Fig. 3(a)], the inhomogeneously constrained magnetic nanoislands in Fig. 3(b) under the same strain condition display a single vortex domain state due to the reduced elastic anisotropy.[15] Such a single vortex domain state has been observed via Magnetic Force Microscope (MFM) in circular permalloy ($Ni_{80}Fe_{20}$) islands of micrometer or submicrometer size,[55] demonstrated in circular supermalloy ($Ni_{80}Fe_{14}Mo_5$) islands of nanometer size via macroscopic magneto-optical Kerr effect (MOKE) measurement,[56] and importantly, with both internal IP vortex domain structure and perpendicular magnetization of the vortex core being directly observed in Fe islands via the sophisticated spin-polarized scanning tunneling microscopy (SP-STM).[57] On the other hand, in continuous magnetic thin films [Fig. 3(c)] upon (-0.5%, -0.5%), the vortex domain exhibits a lattice-like arrangement, i.e., unenclosed and periodic. Such lattices of magnetic vortices in square-shaped, homogeneously constrained continuous magnetoelastic films await experimental confirmation.

Moreover, the simulation results show that the vortices in all three magnetic nanostructures can be manipulated via strain. However, in comparison with the homogeneously constrained nanoscale [Fig. 3(a)] and continuous magnetic thin films [Fig. 3(c)], the domain states in the stress-relaxed

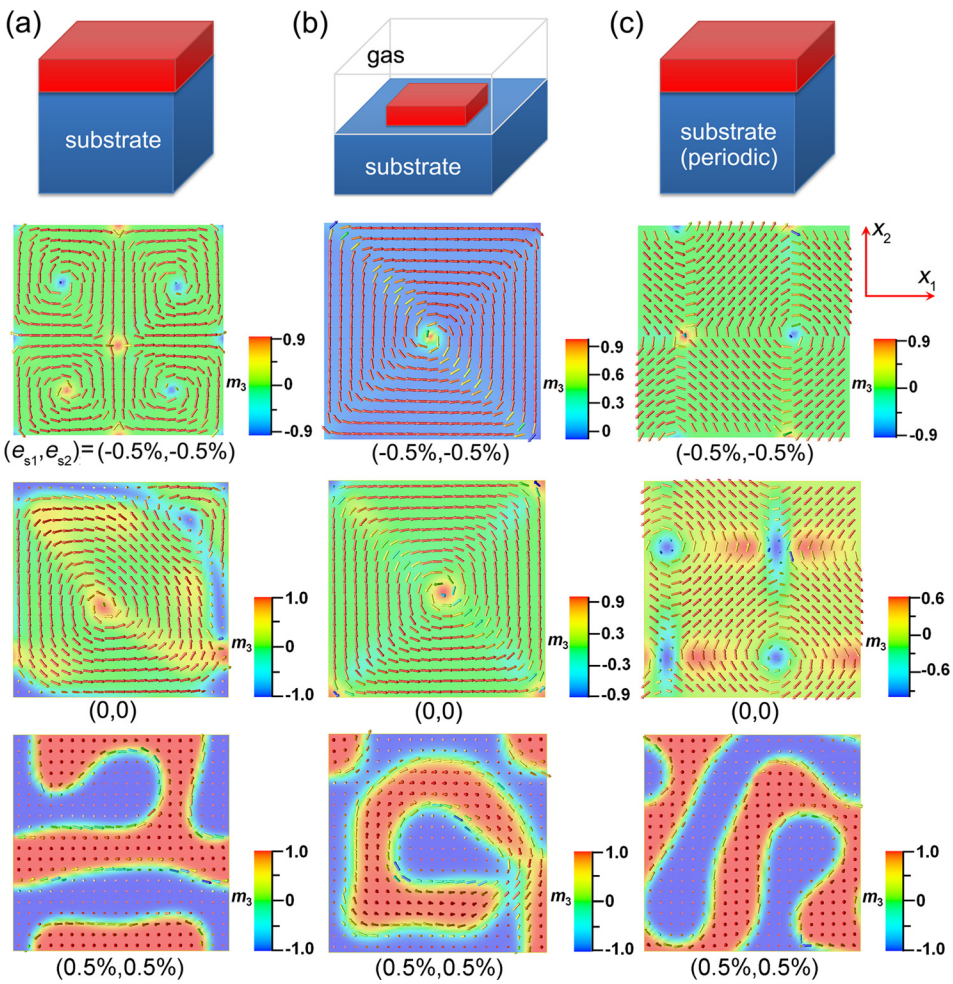

FIG. 3. Vector diagram illustrations (top view) of the vortex domain states in (a) homogeneously constrained nanoscale magnetic thin films with finite-size magnetostatic boundary condition, (b) magnetic nanoislands with finite-size magnetostatic boundary condition and stress-free mechanical boundary conditions along the surfaces, and (c) homogeneously constrained continuous magnetic thin films with periodic magnetostatic boundary condition. The corresponding in-plane strain, i.e., (e_{s1},e_{s2}), are shown. The geometric size of the above three cases is taken as $192 \times 192 \times 35$ nm^3. (Color bar) m_3 indicates the normalized magnetization in the out-of-plane x_3, i.e., the [001] direction.

magnetic nanoislands [Fig. 3(b)] are less sensitive to the strain. For example, the islands upon the compressive and zero IP strains both show single vortex domains [Fig. 3(b)] compared to multiple vortices in the constrained thin films [Figs. 3(a) and 3(c)] under identical strain conditions. This is caused by the reduced elastic energy in isolated islands wherein the actual strain imposed would be smaller due to stress relaxation. Despite such lower strain sensitivity, the applied tensile IP strain of (0.5%, 0.5%) is still sufficient to switch the magnetization OOP even if the magnitude of actual strain should be smaller than it. However, such reduced strain would lead to significantly wider Bloch-type domain walls [Fig. 3(b)] compared to those in constrained thin-film magnets upon identical tensile IP strains [Figs. 3(a) and 3(c)]. Particularly, the micromagnetic simulations without incorporating the elastic contribution[55] would always produce a single vortex domain similarly to that in magnetic nanoislands under zero strain [Fig. 3(b)] and hence cannot precisely predict the strain-stabilized domain structures in nanomagnets.

Furthermore, the magnetic vortices in continuous Ni thin films under zero strain show a coexistence of the IP Néel-type and the OOP Bloch-type domain walls [Fig. 3(c)]. Upon the action of the compressive IP strain of (−0.5%, −0.5%), the IP Néel wall would expand while the OOP Bloch wall would reduce. Such a strain-induced domain wall structure transformation is comparable to the experimental observation via MFM in a continuous Ni film but with a different thickness of 60 nm.[34]

In addition, it is worth noting that the presence of the vortex domain state in magnetic nanoislands is strongly size-dependent, mainly governed by the competing short-range exchange and long-range magnetostatic energy. Figure 4(a) shows the lateral size (i.e., length and width) dependence of the magnetization distribution in magnetic nanoislands with a thickness of 35 nm. It can be seen that the minimum lateral size for the presence of the vortex domain is about 80 nm, i.e., $80 \times 80 \times 35$ nm^3. As the lateral size becomes smaller, the dominative short-range exchange energy would lead to either a uniform single-domain (32 nm) or a buckle-like domain (72 nm). The predicted geometric size-dependent domain morphology transition in stress-relaxed magnetic nanoislands agrees well with previous results based on micromagnetic simulations where the elastic anisotropy is not included,[16,17] demonstrating a wider applicability of our phase-field approach. Nevertheless, such size dependence would be different in homogeneously constrained nanoscale magnetic thin films due to the stronger influence from the elastic strain. Furthermore, it is found that the minimum lateral size for the presence of vortex domain increases with decreasing thickness, as illustrated by the vector diagrams of the magnetic nanoislands with a smaller thickness of 15 nm in Fig. 4(b). As seen, the vortex domain state appears when the lateral size exceeds 88 nm otherwise the island would present either a single-domain (32 nm), leaf-like (72 nm), or buckle-like (80 nm) domain configuration due to the dominative exchange energy.

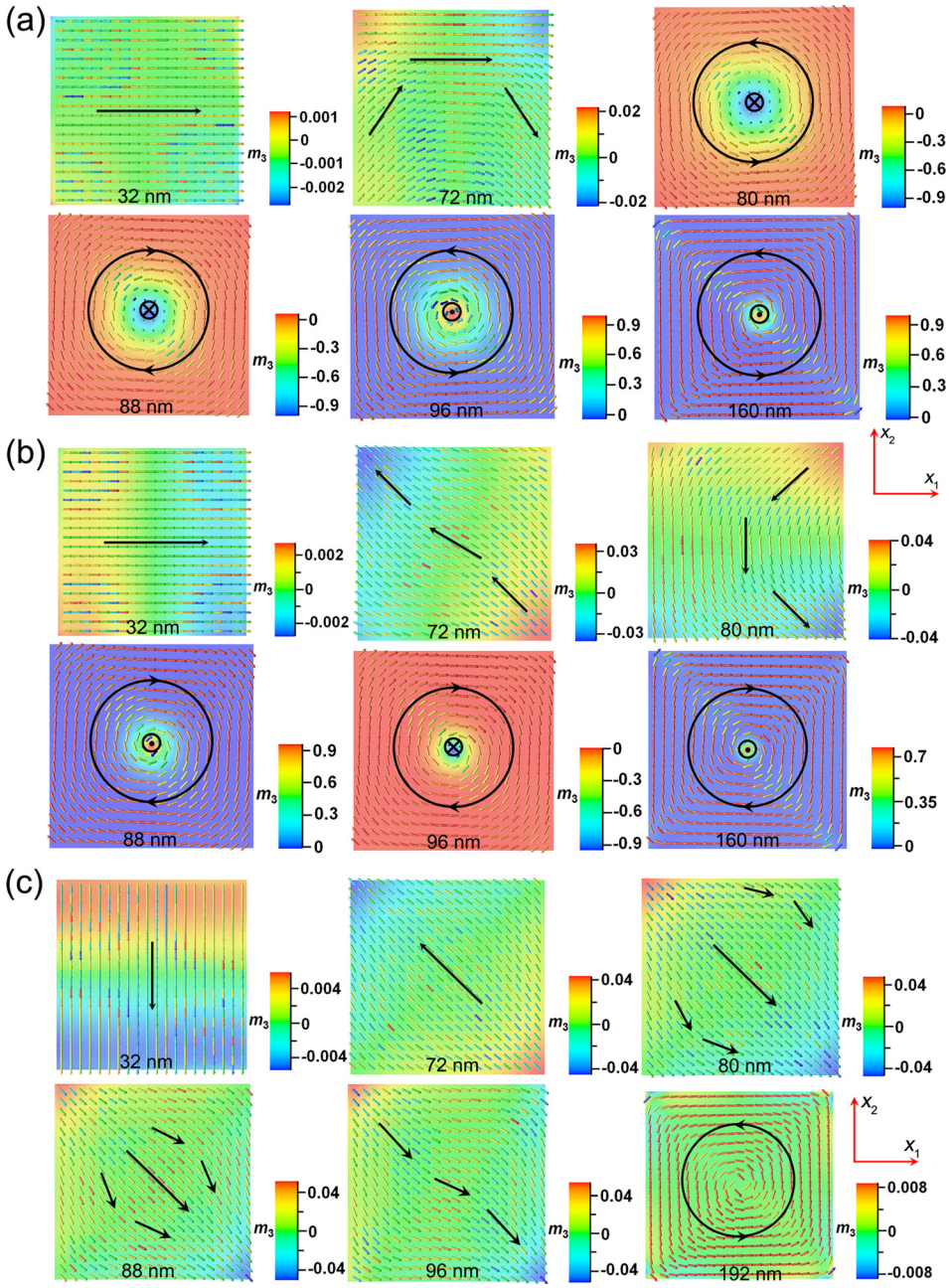

FIG. 4. Lateral size-dependent vector diagram illustrations (top view) of the magnetization distributions in inhomogeneously constrained isolated magnetic nanoislands with thicknesses of (a) 35 nm, (b) 15 nm, and (c) 5 nm, respectively. The arrows and the circles represent the magnetization distribution and the chirality of the vortex domain; the symbols ⊗ and ⊙ indicate the magnetic vectors pointing downwards and upwards, respectively. The average strains (e_{s1}, e_{s2}) herein are taken as (−0.5%, −0.5%). (Color bar) m_3 indicates the normalized magnetization in the out-of-plane x_3, i.e., the [001] direction.

Also note that for both the thicknesses of 35 nm and 5 nm, the chirality of the vortices is prone to change in the vicinity of the critical transition lateral sizes, since the comparable contributions from the exchange and magnetostatic energy would place the magnetic island in an energetically unstable region. For example, in the 35-nm-thick nanoislands, the vortex domain changes from left-handed chirality at the lateral size of 80 nm [i.e., anti-clockwise vector alignment with downward spin direction at the center core, see Fig. 4(a)], to a right-handed one at the larger lateral sizes, e.g., the clockwise vectors with downward center core spins at 88 nm, or the anti-clockwise vector with upward center core spins at both the 96 nm and 160 nm.

The critical lateral size for such stabilized vortex domain further increases to 192 nm when the thickness reduces to 5 nm, as indicated in Fig. 4(c). Such a thickness-dependent transition behavior can be attributed to the enhanced OOP demagnetization energy in smaller thickness islands,[16] which would tend to suppress the vertical spin vectors at the core to the film plane [e.g., the $192 \times 192 \times 15\ \text{nm}^3$ island in Fig. 4(b)] and eventually produce a fully in-plane vortex domain if the demagnetization energy was strong enough, for example, in the $192 \times 192 \times 5\ \text{nm}^3$ island, where the vertical magnetization component m_3 is almost zero even at the center core [see the corresponding vector diagram in Fig. 4(c)].

C. Magnetic domain dynamics under strains

Now let us turn to the dynamics of the strain-driven domain and domain wall structures. Herein the dynamics indicate the time-dependent stabilization of the magnetic domain (wall) structures upon the strains which have already been applied to the magnetic thin film and achieved mechanical

equilibrium. As an example, Figure 5 shows the time-dependent OOP magnetic domain (i.e., *c* domain) switching in homogeneously constrained polycrystalline Ni films of different sizes, induced by isotropic biaxial IP strains. In the single-domain $64 \times 64 \times 35\,\text{nm}^3$ Ni film with a critical switching strain of about 0.29% (calculated based on the formalisms in Ref. 7), the isotropic biaxial strains of 0.75% and 0.95% are sufficient to switch the magnetization vectors OOP. Such a strong elastic driving force would suppress the precessional rotation which is common in single-domain magnets[10] and lead to a fast and smooth magnetization switching. By comparison, the critical OOP switching strain in the thinner $64 \times 64 \times 15\ \text{nm}^3$ film is around 0.68% due to the enhanced demagnetization energy. As a result, the same isotropic biaxial strains of 0.75% and 0.95% provide much smaller elastic driving forces, which would allow remarkable processional switching features and result in significantly longer switching times, i.e., 19.18 and 7.93 ns, respectively [see Fig. 5(a)]. On the other hand, the OOP switching would somewhat be hampered by the presence of domain walls in the multi-domain $192 \times 192 \times 35\ \text{nm}^3$ Ni films with isotropic biaxial strains of 0.75% and 0.95%, as indicated by the smaller volume fractions of the *c* domain [see the top two panels in Fig. 5(b)]. Among them, the strain of 0.95% can provide a stronger driving force which leads to faster switching speed and higher volume fraction of *c* domain than that of 0.75%. In the thinner multi-domain $192 \times 192 \times 15\ \text{nm}^3$ film, the isotropic biaxial strain of 0.75% is insufficient to induce the OOP switching (i.e., almost no *c* domains) due to the enhanced demagnetization, while the strain of 0.95% can successfully rotate the magnetic domains OOP via domain nucleation or domain-wall motion,[11] leading to a fast and smooth switching as well. The critical strain for such OOP switching is around 0.85% at which the volume fraction of *c* domain exceeds 50%.[54] Figure 5(c) illustrates the detailed magnetic vector distributions during the strain-induced dynamic domain switching in single-domain $64 \times 64 \times 35\,\text{nm}^3$ and multi-domain $192 \times 192 \times 35\ \text{nm}^3$ Ni films, which show well-defined coherent rotation and domain-wall motion behaviors, respectively.

IV. CONCLUSIONS

In summary, we investigated the strain effects on magnetic domain stability and dynamics in nanoscale magnetic thin films using phase-field simulations. A strain-domain stability map was constructed for homogeneously constrained nanoscale magnetic thin films, which displays numerous magnetic domain states stabilized by isotropic and anisotropic biaxial strains including a circular IP vortex domain. Such magnetic vortices can also present in stress-relaxed magnetic nanoislands with a strong lateral size dependence. In continuous magnetic thin films, the vortex domain exhibits an unenclosed and periodic (lattice-like) behavior. Domain structures in all the three magnetic nanostructures can be effectively engineered via strain.

Given that future development in large-scale on-chip integration of multifunctional components requires the growth of nanoscale magnetic thin films partially or fully constrained on a substrate, the present results provide theoretical basis for the experimental observation of the domain structures in thin-film nanomagnets with different mechanical boundary conditions. The established strain-domain stability map provides useful guidelines for a precise control over magnetic domain structures. Finally, it is worth noting that the strain and

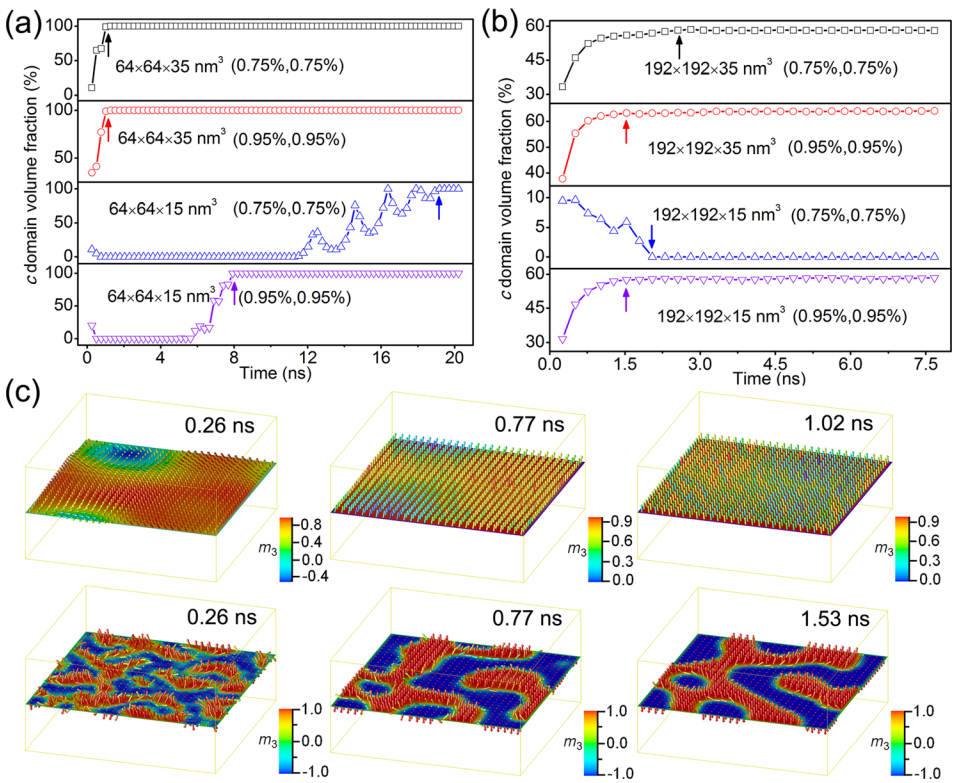

FIG. 5. Dynamics of the out-of-plane *c* domain switching upon the biaxial in-plane strains along the x_1 and x_2 axes, i.e., (e_{s1},e_{s2}), in (a) single-domain $64 \times 64\,\text{nm}^2$ and (b) multi-domain $192 \times 192\,\text{nm}^2$ homogeneously constrained magnetic thin films of different thicknesses. The arrows indicate the time when the domain evolution achieves equilibrium. (c) Vector diagram illustrations of the time-dependent domain evolution in (the first row) $64 \times 64 \times 35\,\text{nm}^3$ and (the second row) $192 \times 192 \times 35\ \text{nm}^3$ homogeneously constrained magnetic thin films with $e_{s1} = e_{s2} = 0.95\%$.

corresponding mechanical boundary condition are important for almost all structural transformations, of interests in other branches such as ferroelectric,[58] flexoelectric,[59] flexomagnetic,[60] multiferroic,[61,62] and strong correlated materials and systems.[63–65] Under such circumstances, the present phase-field approach would manifest itself as a useful tool in understanding the strain effect on the microstructure evolution of single-phase/composite materials under complex boundary conditions, which would enable novel strain-engineered coupling behaviors (e.g., flexomagnetoelectric[66]) at the nanoscale.

ACKNOWLEDGMENTS

This work was supported by the NSF of China (Grant Nos. 51332001, 51221291, and 11234005), the National Basic Research Program of China (Grant No. 2009CB623303), and the NSF (Grant No. DMR-1006541). The computer simulations were carried out on the LION and Cyberstar clusters at the Pennsylvania State University supported in part by NSF Major Research Instrumentation Program through grant OCI-0821527 and in part by the Materials Simulation Center and the Graduated Education and Research Services at the Pennsylvania State University.

[1]A. G. Khachaturyan, *Theory of Structural Transformation in Solids* (Wiley, New York, 1983).
[2]D. G. Schlom, L. Q. Chen, C. B. Eom, K. M. Rabe, S. K. Streiffer, and J. M. Triscone, Annu. Rev. Mater. Res. **37**, 589 (2007).
[3]J. H. Haeni, P. Irvin, W. Chang, R. Uecker, P. Reiche, Y. L. Li, S. Choudhury, W. Tian, M. E. Hawley, B. Craigo, A. K. Tagantsev, X. Q. Pan, S. K. Streiffer, L. Q. Chen, S. W. Kirchoefer, J. Levy, and D. G. Schlom, Nature **430**, 758 (2004).
[4]K. J. Choi, M. Biegalski, Y. L. Li, A. Sharan, J. Schubert, R. Uecker, P. Reiche, Y. B. Chen, X. Q. Pan, V. Gopalan, L. Q. Chen, D. G. Schlom, and C. B. Eom, Science **306**, 1005 (2004).
[5]G. Sheng, J. M. Hu, J. X. Zhang, Y. L. Li, Z. K. Liu, and L. Q. Chen, Acta Mater. **60**, 3296 (2012).
[6]N. A. Pertsev, Phys. Rev. B **78**, 212102 (2008).
[7]J.-M. Hu and C. W. Nan, Phys. Rev. B **80**, 224416 (2009).
[8]J.-M. Hu, Z. Li, J. Wang, and C. W. Nan, J. Appl. Phys. **107**, 093912 (2010).
[9]J.-M. Hu, Z. Li, J. Wang, J. Ma, Y. H. Lin, and C. W. Nan, J. Appl. Phys. **108**, 043909 (2010).
[10]J.-M. Hu, Z. Li, L.-Q. Chen, and C.-W. Nan, Nat. Commun. **2**, 553 (2011).
[11]J.-M. Hu, Z. Li, L.-Q. Chen, and C.-W. Nan, Adv. Mater. **24**, 2869 (2012).
[12]M. Liu, Z. Zhou, T. Nan, B. M. Howe, G. J. Brown, and N. X. Sun, Adv. Mater. **25**, 1435 (2013).
[13]M. Liu, O. Obi, J. Lou, Y. J. Chen, Z. H. Cai, S. Stoute, M. Espanol, M. Lew, X. Situ, K. S. Ziemer, V. G. Harris, and N. X. Sun, Adv. Funct. Mater. **19**, 1826 (2009).
[14]C. A. F. Vaz, J. Hoffman, C. H. Ahn, and R. Ramesh, Adv. Mater. **22**, 2900 (2010).
[15]C. Kittel. Rev. Mod. Phys. **21**, 541 (1949).
[16]R. P. Cowburn and M. E. Welland, Phys. Rev. B **58**, 9217 (1998).
[17]R. P. Cowburn and M. E. Welland, Appl. Phys. Lett. **72**, 2041 (1998).
[18]V. Nagarajan, A. Roytburd, A. Stanishevsky, S. Prasertchoung, T. Zhao, L. Chen, J. Melngailis, O. Auciello, and R. Ramesh, Nat. Mater. **2**, 43 (2003).
[19]T. K. Chung, S. Keller, and G. P. Carman. Appl. Phys. Lett. **94**, 132501 (2009).
[20]J. X. Zhang and L. Q. Chen, Acta Mater. **53**, 2845 (2005).
[21]J. X. Zhang and L. Q. Chen, Philos. Mag. Lett. **85**, 533 (2005).
[22]C. Israel, N. D. Mathur, and J. F. Scott, Nat. Mater. **7**, 93 (2008).
[23]M. Ghidini, R. Pellicelli, J. L. Prieto, X. Moya, J. Soussi, J. Briscoe, S. Dunn, and N. D. Mathur, Nat. Commun. **4**, 1453 (2013).
[24]T. Wu, A. Bur, P. Zhao, K. P. Mohanchandra, K. Wong, K. L. Wang, C. S. Lynch, and G. P. Carman, Appl. Phys. Lett. **98**, 012504 (2011).
[25]J. Walowski, M. D. Kaufmann, B. Lenk, C. Hamann, J. McCord, and M. Münzenberg, J. Phys. D: Appl. Phys. **41**, 164016 (2008).
[26]R. F. L. Evans, D. Hinzke, U. Atxitia, U. Nowak, R. W. Chantrell, and O. Chubykalo-Fesenko, Phys. Rev. B **85**, 014433 (2012).
[27]U. Atxitia, P. Nieves, and O. Chubykalo-Fesenko, Phys. Rev. B **86**, 104414 (2012).
[28]T. A. Ostler, J. Barker, R. F. L. Evans, R. W. Chantrell, U. Atxitia, O. Chubykalo-Fesenko, S. El Moussaoui, L. Le Guyader, E. Mengotti, L. J. Heyderman, F. Nolting, A. Tsukamoto, A. Itoh, D. Afanasiev, B. A. Ivanov, A. M. Kalashnikova, K. Vahaplar, J. Mentink, A. Kirilyuk, T. Rasing, and A. V. Kimel, Nat. Commun. **3**, 666 (2012).
[29]S. C. Seel, C. V. Thompson, S. J. Hearne, and J. A. Floro, J. Appl. Phys. **88**, 7079 (2000).
[30]J. A. Floro, E. Chason, R. C. Cammarata, and D. J. Srolovitz, MRS Bull. **27**, 19 (2002).
[31]L. Q. Chen, J. Am. Ceram. Soc. **91**, 1835 (2008).
[32]C. Thiele, C. K. Dörr, O. Bilani, J. Rödel, and L. Schultz, Phys. Rev. B **75**, 054408 (2007).
[33]S. Zhang, Y. G. Zhao, P. S. Li, J. J. Yang, S. Rizwan, J. X. Zhang, J. Seidel, T. L. Qu, Y. J. Yang, Z. L. Luo, Q. He, T. Zou, Q. P. Chen, J. W. Wang, L. F. Yang, Y. Sun, Y. Z. Wu, X. Xiao, X. F. Jin, J. Huang, C. Gao, X. F. Han, and R. Ramesh, Phys. Rev. Lett. **108**, 137203 (2012).
[34]C.-J. Hsu, J. L. Hockel, and G. P. Carman, Appl. Phys. Lett. **100**, 092902 (2012).
[35]S. E. Park and T. R. Shrout, J. Appl. Phys. **82**, 1804 (1997).
[36]A. N. Stroh, J. Math. Phys. **41**, 77 (1962).
[37]J. X. Zhang, R. Wu, S. Choudhury, Y. L. Li, S. Y. Hu, and L. Q. Chen, Appl. Phys. Lett. **92**, 122906 (2008).
[38]S. Y. Hu and L. Q. Chen, Acta Mater. **49**, 1879 (2001).
[39]P. Yu, S. Y. Hu, L. Q. Chen, and Q. Du, J. Comput. Phys. **34**, 208 (2005).
[40]M. E. Schabes and A. Aharoni, IEEE Trans. Magn. **23**, 3882 (1987).
[41]C. A. F. Vaz, J. A. C. Bland, and G. Lauhoff, Rep. Prog. Phys. **71**, 056501 (2008).
[42]X. P. Wang, C. J. García-Cervera, and E. Weinan, J. Comput. Phys. **171**, 357 (2001).
[43]J.-M. Hu, C.-W. Nan, and L.-Q. Chen, Phys. Rev. B **83**, 134408 (2011).
[44]J.-M. Hu, T. N. Yang, L. Q. Chen, and C. W. Nan, J. Appl. Phys. **113**, 194301 (2013).
[45]T. H. E. Lahtinen, K. J. A. Franke, and S. van Dijken, Sci. Rep. **2**, 258 (2012).
[46]T.-K. Chung, G. P. Carman, and K. P. Mohanchandra, Appl. Phys. Lett. **92**, 112509 (2008).
[47]Z. Wang, R. Viswan, B. Hu, J.-F. Li, V. G. Harris, and D. Viehland, J. Appl. Phys. **111**, 034108 (2012).
[48]T. Brintlinger, S.-H. Lim, K. H. Baloch, P. Alexander, Y. Qi, J. Barry, J. Melngailis, L. Salamanca-Riba, I. Takeuchi, and J. Cumings, Nano Lett. **10**, 1219 (2010).
[49]R. V. Chopdekar, V. K. Malik, A. Fraile Rodríguez, L. Le Guyader, Y. Takamura, A. Scholl, D. Stender, C. W. Schneider, C. Bernhard, F. Nolting, and L. J. Heyderman, Phys. Rev. B **86**, 014408 (2012).
[50]R. Streubel, D. Köhler, R. Schäfer, and L. M. Eng, Phys. Rev. B **87**, 054410 (2013).
[51]R. C. O'Handley, O. S. Song, and C. A. Ballentine, J. Appl. Phys. **74**, 6302 (1993).
[52]A. Lyberatos and R. W. Chantrell, J. Appl. Phys. **73**, 6501 (1993).
[53]A. Lyberatos, D. V. Berkov, and R. W. Chantrell, J. Phys.: Condens. Matter **5**, 8911 (1993).
[54]See supplementary material at http://dx.doi.org/10.1063/1.4826491 for more discussion on the thermal stability; corresponding domain structures in the Ni film of $192 \times 192 \times 15$ nm^3; vector diagrams of domain wall structures; and illustrations of the time-dependent domain evolutions.
[55]T. Shinjo, T. Okuno, R. Hassdorf, K. Shigeto, and T. Ono, Science **289**, 930 (2000).
[56]R. P. Cowburn, D. K. Koltsov, A. O. Adeyeye, M. E. Welland, and D. M. Tricker, Phys. Rev. Lett. **83**, 1042 (1999).
[57]A. Wachowiak, J. Wiebe, M. Bode, O. Pietzsch, M. Morgenstern, and R. Wiesendanger, Science **298**, 577 (2002).
[58]G. Sheng, J. X. Zhang, Y. L. Li, S. Choudhury, Q. X. Jia, Z. K. Liu, and L. Q. Chen, Appl. Phys. Lett. **93**, 232904 (2008).
[59]D. Lee, A. Yoon, S. Y. Jang, J. G. Yoon, J. S. Chung, M. Kim, J. F. Scott, and T. W. Noh, Phys. Rev. Lett. **107**, 057602 (2011).
[60]E. A. Eliseev, A. N. Morozovska, M. D. Glinchuk, and R. Blinc, Phys. Rev. B **79**, 165433 (2009).
[61]R. J. Zeches, M. D. Rossell, J. X. Zhang, A. J. Hatt, Q. He, C.-H. Yang, A. Kumar, C. H. Wang, A. Melville, C. Adamo, G. Sheng, Y.-H. Chu,

J. F. Ihlefeld, R. Erni, C. Ederer, V. Gopalan, L. Q. Chen, D. G. Schlom, N. A. Spaldin, L. W. Martin, and R. Ramesh, Science **326**, 977 (2009).
[62]J. H. Lee, L. Fang, E. Vlahos, X. Ke, Y. W. Jung, L. F. Kourkoutis, J.-W. Kim, P. J. Ryan, T. Heeg, M. Roeckerath, V. Goian, M. Bernhagen, R. Uecker, P. C. Hammel, K. M. Rabe, S. Kamba, J. Schubert, J. W. Freeland, D. A. Muller, C. J. Fennie, P. Schiffer, V. Gopalan, E. Johnston-Halperin, and D. G. Schlom, Nature **466**, 954 (2010).
[63]K. H. Ahn, T. Lookman, and A. R. Bishop, Nature **428**, 401 (2004).
[64]Q. P. Chen, J. J. Yang, Y. G. Zhao, S. Zhang, J. W. Wang, M. H. Zhu, Y. Yu, X. Z. Zhang, Z. Wang, B. Yang, D. Xie, and T. L. Ren, Appl. Phys. Lett. **98**, 172507 (2011).
[65]Y. Gu, J. Cao, J. Wu, and L.-Q. Chen, J. Appl. Phys. **108**, 083517 (2010).
[66]E. A. Eliseev, M. D. Glinchuk, V. Khist, V. V. Skorokhod, R. Blinc, and A. N. Morozovska, Phys. Rev. B **84**, 174112 (2011).